Mesoporous H-ZSM-5 for the Conversion of Dimethyl Ether to Hydrocarbons

Michael C. Zimmermann*, Thomas N. Otto*, Simon Wodarz, Thomas A. Zevaco, and Stephan Pitter

DOI: 10.1002/cite.201800217

Supporting Information available online

The potential of hierarchical H-ZSM-5 zeolites was studied for the conversion of DME to fuel-compatible hydrocarbons. For this purpose, hierarchical H-ZSM-5 zeolites have been prepared from commercial H-ZSM-5 by desilication and organosilane-directed hydrothermal synthesis. The zeolites were characterized by X-ray diffraction, NH_3-TPD, DRIFTS, and N_2 physisorption measurements. The catalysts have been tested in a tube reactor (1 bar, 648 K). The results indicate important structural changes in framework and acidic sites, which are significant for the synthesis of gasoline-range hydrocarbons.

Keywords: Desilication, Dimethyl ether, DRIFTS, Gasoline, Hierarchical H-ZSM-5, Temperature-programmed desorption

Received: December 03, 2018; *revised:* July 03, 2019; *accepted:* July 10, 2019

1 Introduction

A promising capability for a sustainable fuel production arises by linking raw materials derived from renewable resources with an innovative DtG process (dimethyl ether to gasoline) [1, 2]. One example for such a BtL application (biomass to liquids) is the Karlsruhe bioliq® process [3]. The synthesis of fuel by means of converting biogenic dimethyl ether over a H-ZSM-5 zeolite catalyst is the last step of the bioliq® process. The DtG process corresponds to the thoroughly investigated MtG process (methanol to gasoline) in many respects. As the dehydration of methanol is taking place upstream to the gasoline synthesis step, the conversion of dimethyl ether (DME) to hydrocarbons is less exothermic. Furthermore, DME conversion enhances the carbon efficiency compared to methanol conversion [4 – 6]. Since the 1970s H-ZSM-5 has been well investigated and established for this reaction because of the low coking tendency and an adequate product distribution [7, 8]. An optimization of the microporous material ZSM-5 can be achieved by introducing meso- and/or macropores, resulting in a so-called hierarchic pore system. Therefore, a wide range of synthesis methods was developed [9 – 13]. One of them is desilication, a demetallation (top-down) approach [14] and another one is the organosilane-directed hydrothermal synthesis (bottom-up approach) [15].

The hierarchical pore structure is supposed to counteract the disadvantage of diffusion limitations in a purely microporous pore system [16 – 18]. The aim is a molecular traffic control within the catalyst particle to tailor the selectivity. Furthermore, it was shown that a mesoporous superstructure resulted in remarkably prolonged lifetimes for zeolites in a variety of catalytic applications. A relationship between pore connectivity and coking properties was described in literature [19]. The influence of the change of the different acid sites on the reaction, which is due to the different synthetic methods [20, 21] is still unclear.

Furthermore, different calcination procedures affect the acidity and as a consequence the catalytic behavior [22]. In this context it is important to stress the previously described finding that acid centers are not located within the mesopores [23]. Janssens has developed a model for comparing and interpreting curves of methanol conversion as a function of time on stream (*TOS*) for MtG experiments [24]. This allows the determination of a deactivation and activity coefficient and is herein adapted to the DtG process.

Commercial microporous H-ZSM-5 as well as derived desilicated, organosilane-based and the combination of both

Dr. Michael C. Zimmermann, Dr. Thomas N. Otto, Simon Wodarz, Dr. Thomas A. Zevaco, Dr. Stephan Pitter
Michael.zimmermann@kit.edu
thomas.otto@kit.edu
Karlsruher Institut für Technologie (KIT), Institut für Katalyseforschung und -technologie (IKFT), Hermann-von-Helmholtz Platz 1, 76344 Eggenstein-Leopoldshafen, Germany.

methods were compared. The diffuse reflectance infrared Fourier transform (DRIFT) spectroscopy combined with desorption of NH_3 is an additional approach to get a deeper insight of the different weak and strong acid sides. The Si/Al ratio was determined from the optical emission spectrometry (ICP-OES). N_2-physisorption isotherms were measured for the characterization of the catalysts, temperature-programmed desorption curves of NH_3 were prepared, and powder diffraction patterns were recorded. Long-term experiments were performed in a tube reactor under carefully selected conditions to provoke a minimum thermal gradient over the catalyst bed. The products (gasoline range) have been analyzed by gas chromatography and, furthermore, conversion curves were fitted with the Janssens model to determine activity and deactivation coefficients.

2 Methods and Calculations

In the following the methods and calculations for catalyst characterization (powder X-ray diffraction (PXRD), DRIFTS, temperature-programmed desorption of ammonia (NH_3-TPD), N_2 physisorption) are explained. Furthermore, the regulations for catalyst preparation and catalyst testing are explained. Finally, the calculation according to the Janssens model is presented.

2.1 Powder X-ray Diffraction

Diffractograms were recorded at 298 K on a PANalytical X'Pert PRO instrument using Cu Kα radiation. Powdered and grinded samples (20 – 25 mg) were measured on a zero signal sample holder (Si single crystal) in the range 5 – 80° 2θ over 2 h with a step size of 0.0167°. Data analysis was carried out using Highscore Plus (version 3.0.4). Crystallinity was determined by comparison with the commercial samples CBV5524G (A) and CBV8014 (B), respectively, with assumed crystallinities of 100 %. The relative crystallinity (SI_{XRD}) of the products was determined from data in the range of 5° to 40° 2θ and the sum of the counting pulses according to Eq. (1).

$$SI_{XRD} = \frac{S_x}{S_r} \cdot 100 \quad (1)$$

S_x is the sum of the counting pulses of the sample signals, and S_r is the sum of the counting pulses of the reference signals.

2.2 Temperature-Programmed Desorption of Ammonia

NH_3-TPD was performed at ambient pressure (Micromeritics AutoChem HP 2950) with 100 – 200 mg of powdered zeolite in a double-legged quartz tube, heated to 450 °C (2 K min^{-1}) in a He carrier gas stream (30 mL min^{-1}) and dried for 130 min. After cooling, sample loading was carried out with NH_3 (5 % NH_3 in He, 30 mL min^{-1}) at 100 °C for 60 min. Desorption of the physisorbed NH_3 takes place under He (30 mL min^{-1}) at 120 °C for 100 min. The sample was then heated to 450 °C (4 K min^{-1}) and held at this temperature for 60 min followed by further heating to 750 °C (4 K min^{-1}) and cooled down to 120 °C (rate 10 K min^{-1}). NH_3 concentration is determined by calculation from the signals using a mass spectrometer (Cirrus2, MKS Instruments UK Ltd.) with the ion masses to charge ratios m/z 17 and m/z 18 to eliminate the influence of residual H_2O.

2.3 Inductively Coupled Plasma Optical Emission Spectrometry

The ICP-OES were carried out on an Agilent 725 ICP-OES spectrometer. As evaluation software, Agilent Vista Pro ICP-OES, National Instruments Corporation, was used. A multi-element standard for the analysis (SCP Sciena, standard plasma CAL 701-021-53) was applied. For sample pretreatment, about 20 mg of powdered zeolite are dissolved in 1 mL HF (ω_i = 40 % in H_2O) in a flask over at least 12 h.

2.4 Diffuse Reflectance Infrared Fourier Transform Spectroscopy

DRIFT spectra were recorded on a Bruker Vertex 70 FTIR spectrometer (software Opus 6.5) by means of a diffuse reflection chamber as auxiliary equipment (Praying Mantis, Co. Harrick). Samples were pressed, milled and sieved (sieve fractions between 80 µm and 212 µm), then heated for 1 h under He flow (50 mL min^{-1}) at 500 °C. After cooling to 50 °C, the first DRIFT spectrum was recorded. Subsequently, a gas flow with NH_3 (φ_i = 5 % NH_3 in He, 50 mL min^{-1}) is passed through the cell at 50 °C. After about 0.5 h, gas flow is changed to pure He (50 mL min^{-1}). The mass signal m/z 17 is tracked and when the signal is expiring a DRIFT spectrum is recorded. Before recording DRIFT spectra, the samples were heated for approx. 10 min to 150 °C, 250 °C, 350 °C, and 450 °C in order to desorb NH_3. For each of these temperatures a DRIFT spectrum at 50 °C was recorded under pure He flow (50 mL min^{-1}). Kubelka-Munk (KM) functions are derived from KBr background (S_{KBr}) and sample spectra (S_{sample}) according to Eq. (2).

$$KM = \frac{\left(1 - \frac{S_{sample}}{S_{KBr}}\right)^2}{2\left(\frac{S_{sample}}{S_{KBr}}\right)} \quad (2)$$

2.5 N_2 Physisorption

N_2 physisorption measurements (Autosorb IQ and Nova 2000e, Quantachrome) were carried out under isothermal

conditions (N_2, –196.15 °C). BET according to DIN ISO 9277 [25], t-plot according to DIN 66-135-2 [26], and BJH methods according to DIN 66134 [27] are used for evaluation (ASiQwin version 3.01, Quantachrome).

2.6 Catalyst Preparation

For the tests, desilicated zeolites A1, B1, A1RK were prepared (1). Furthermore, a hierarchical ZSM-5 was obtained by the method of Choi et al. [15] via hydrothermal synthesis with the addition of an organosilane (ZS16) and additionally desilicated (ZS16D) (2).

1) Catalysts prepared by desilication [14] are based on commercial ZSM-5 materials (Zeolyst Int.), CBV5524G (A) and CBV8014 (B). 10 g of powdered NH_4-ZSM-5 is suspended in 250 mL of 0.1 M NaOH solution (A1, A1RK, B1) at 60 °C for 30 min. The reaction mixture is then cooled down (< 10 °C). The suspension is centrifuged, and the solid residue is washed three times with distilled H_2O. The ion exchange is carried out by stirring in 0.1 M NH_4NO_3 solution, subsequent washing with H_2O, and drying at 90 °C for 24 h. Calcination is carried out for 10 h at 530 °C (heating rate 1.2 K min^{-1}). A1 and B1 were calcined under air, and A1RK under Ar. The sequence of ion exchange, washing, drying and calcination is carried out three times in total.
2) Template synthesis is carried out with the addition of the mesopore-directing template [3-(trimethoxysilyl)-propyl]hexadecyldimethylammonium chloride (TPHAC). For the synthesis of ZS16, a mixture of Al_2O_3, TPABr, Na_2O, SiO_2, TPHAC and H_2O (molar composition of 1:11:17:61:1.8:7900) is hydrothermally treated at a temperature of 170 °C in a PTFE-coated autoclave for 72 h. The crude product is filtered off and washed with H_2O. The residue is dried at 90 °C and then calcined and ion-exchanged as described under (1). To obtain catalyst ZS16D, ZS16 is desilicated with 0.1 M NaOH solution at 60 °C for 20 min and after this treated as described in section (1).

2.7 Catalyst Testing

The basic components of the laboratory plant are a DME bottle (Linde, quality 3.5), a HPLC pump (Compact, Bischoff), a mass flow controller (Bronkhorst) for Ar, a tube reactor (inner diameter 8 mm, length 18 cm), and cooling traps. For the analysis of the products a gas chromatograph (Agilent GC 6890) equipped with two columns (Rxi-1ms, Rt-QS-Bond, Restek) and a flame ionization detector (FID) was used.

The HPLC pump conveys liquid dimethyl ether into the plant where it is vaporized and mixed with a preheated Ar flow (140 mL min^{-1}). Subsequently the stream of gas flows over the catalyst bed (200 mg powdery zeolite embedded in 3 g inert SiC) inside the tube reactor. A metal sleeve allows the continuous measurement of the temperature profile with a thermocouple (type K). The heating is realized by two half shells (Al), each fitted with three heating cartridges (Horst GmbH, No. 511161, 230 V, 400 W, max. 1023 K). The experiments were performed at atmospheric pressure at a temperature of 648 K. The weight hourly space velocity (*WHSV*) was 3.3 $g_{DME}g_{cat}^{-1}h^{-1}$. The evaluation of the GC signals of the hydrocarbons was performed with the software Agilent GC ChemStation, Rev. A. 10.02. The background is previously eliminated by subtracting a blank measurement and considering the integral areas of individual FID signals or FID signal ranges (sum of the FID signals of C4+, MeOH, C5, C6 – C9, C10+) in order to calculate the DME conversion X_{DEM} and product selectivities S_{prod} (see Supporting Information, SI).

2.8 Calculation by Janssens' Model

The empirical model of Janssens describes the deactivation of zeolite catalysts in the MtG process [24] and is adopted for the DtG experiments in this work. By the way, it can be assumed that both the DtG process as well as the MtG process are based on the dual-cycle concept. The assumption for the model of Janssens is a first-order reaction and the decrease of activity is proportional to decreasing methanol conversion *X*. Eq. (3) shows the found mathematical relation.

$$X = \frac{\left(\exp\left(k\tau_{mod,0}\right) - 1\right)\exp(-kat)}{1 + \left(\exp\left(k\tau_{mod,0}\right) - 1\right)\exp(-kat)} \tag{3}$$

The rate coefficient *k* provides a dimension of the catalyst activity. The deactivation coefficient *a* describes the deactivation characteristics, and *t* is the reaction time (*TOS*). The modified residence time $\tau_{mod,0}$ shown in Eq. (4) is assumed to be constant in the initial period. m_{cat} corresponds to the catalyst mass and V_{total} to the total volume flow.

$$\tau_{mod,0} = \frac{m_{cat}}{V_{total}} \tag{4}$$

Due to the symmetry of the function (Eq. (3)), an estimation of the conversion capacity R_0 for the experimentally found curves can be made by multiplying the *WHSV* with the reaction time at which a methanol conversion of 50 % is reached. This point in time is, according to the model, independent of the activity of the catalyst and defined by the deactivation coefficient *a*.

3 Results and Discussion

The subsequent discussion focuses on the very complex interplay of all catalytically active parameters in their entirety, which is the actual driving force behind the conversion of dimethyl ether into hydrocarbons.

3.1 Characterization of Catalysts

All X-ray diffractograms show the characteristics of the ZSM-5 diffraction pattern (Fig. 1). Compared to the reference materials A and B the crystallinity of the desilicated zeolites A1 and B1 is increased. One explanation is the release of amorphous components from the starting material. However, since intensities of the reflexes are depending on many variables like the structure factor, temperature, strain, crystal size and others, the following causes are considered for the changes of the reflex intensities:

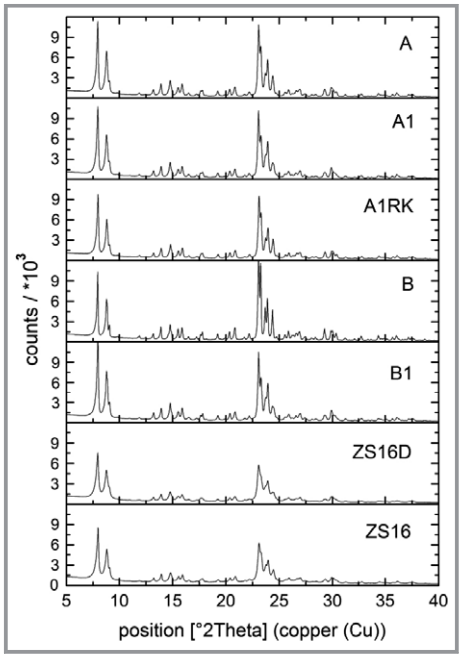

Figure 1. X-ray diffractograms of the calcined powders of A, A1, A1RK, B, B1, ZS16D, and ZS16.

- diminution of defect sites,
- preferred depletion of atoms on certain lattice positions,
- additional molecules or ions present (H_2O, Na^+, NH_4^+, etc.).

B1 shows an increased intensity for the reflection [011] at 7.9° 2θ compared to B, probably related to oxygen atoms located in this diffracting plane, which have been impaired in their position by defect sites (see SI, Figs. S9 and S10). A decrease of defect sites is expectable after alkaline treatment [28]. Reduced intensities of individual reflections can be expected if the number of atoms on certain lattice positions is decreased.

For the laboratory plant experiments the degree of crystallinity must be taken into account, since only the crystalline component is relevant for catalytic activity. This applies, in particular, to the synthesis-related lower crystallinity in the catalysts ZS16 and ZS16D [21]. In contrast to A1RK, the last two mentioned catalysts also follow the trend of increasing crystallinity values after desilication with 0.1 M NaOH solution.

From the NH_3 desorption curves, information is obtained about the alteration of the acidic sites. Desorption curves of all zeolites (Fig. 2) show three regions, the low-temperature range ($NH_{3,LTR}$) followed by the so-called high-temperature range ($NH_{3,HTR}$) and the temperature range above 450 °C ($NH_{3,>450}$). The maxima of $NH_{3,LTR}$ are observed around 200 °C and those of $NH_{3,HTR}$ in the range between 350 °C and 400 °C. Above 450 °C, only minor NH_3 desorption takes place.

The calculated molar Al fractions (Tab. 1) are based on the Si/Al ratios from ICP-OES measurements and the empirical formula of H-ZSM-5 ($H_nAl_nSi_{96-n}O_{192}$). The

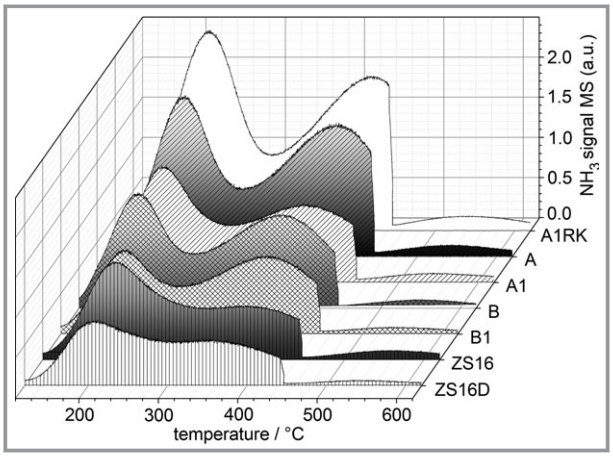

Figure 2. NH_3-TPD signals of all tested zeolites plotted against the temperature.

Table 1. Values of crystallinity (SI_{XRD}), Si/Al ratio, aluminum mass fraction (m(Al)), and NH_3 desorption data (derived from NH_3-TPD experiments).

Sample	SI_{XRD} a) [%]	Si/Al b) [–]	m(Al) c) [µmol g^{-1}]	$NH_{3,tot}$ d) [µmol g^{-1}]	$NH_{3,LTR}$ e) [µmol g^{-1}]	$NH_{3,HTR}$ f) [µmol g^{-1}]	$NH_{3,>450}$ g) [µmol g^{-1}]
A	100	27	601	662	274	358	30
A1	102	31	517	462	212	221	28
B	100	37	433	470	198	255	17
B1	112	40	409	386	153	214	19
A1RK	93	21	746	882	350	500	31
ZS16	80	29	566	372	200	147	25
ZS16D	82	16	979	270	138	119	13

a) Cristallinity calculated from XRD signal intensity in the range 5 to 40° 2θ. Values above 100 % cristallinity are practically impossible, however, were recorded unchanged as they are based on a relative comparison to the respective standard. b) Si/Al molar ratio from ICP-OES measurements; c) calculated from Si/Al molar ratio with $H_nAl_nSi_{96-n}O_{192}$ as empirical formula of H-ZSM-5; d) desorbed NH_3, total amount; e) desorbed NH_3, low temperature range; f) desorbed NH_3, high-temperature range; g) desorbed NH_3, above 450 °C.

unmodified commercial H-ZSM-5 (A, B) show a good agreement of the total desorbed NH_3 ($NH_{3,tot}$) regarding their calculated Al values: The values of $NH_{3,tot}$ are slightly above the calculated Al content, which can be explained by multiple adsorption of NH_3 at an acidic aluminum center or chemisorption of NH_3 at other sites.

For A1 ($NH_{3,tot}$ = 462 µmol g^{-1}) a reduction of $NH_{3,tot}$ compared with A ($NH_{3,tot}$ = 662 µmol g^{-1}) takes place. The ratio of $NH_{3,tot}/m$(Al) is lower for A1 (0.89) than for A (1.10), corresponding to a fraction of Al species A1 not interacting with NH_3. In general, reduction of the number of acidic centers by demetallation, the desilication process in this case, is plausible if either pore blocking, transformation of acidic Al centers into non-active species, or loss of Al species takes place.

Also, calcination considerably contributes to changes of the Si/Al ratio as the results for zeolites A1 and A1RK illustrate. The only difference between these two zeolites is the repeated calcination under inert gas (Ar) in the case of A1RK whereas the multiple calcination of A1 was performed in air. Values connected to the Al content (m(Al), $NH_{3,tot}$, $NH_{3,LTR}$, $NH_{3,HTR}$, $NH_{3,>450}$) are increased for A1RK compared to those of A1, which is presumably caused by a varied decomposition of NH_4NO_3 which remained inside the pores after the ion-exchange process. Free aluminum species are lost during washing processes.

For ZS16, the Al concentration of the synthesis mixture and the calculated molar Al fraction (566 µmol g^{-1}) is comparatively high regarding the low value of $NH_{3,tot}$ (372 µmol g^{-1}). Similar to A1 and B1, the NH_3-TPD curve of ZS16D shows reduced values for all three regions of desorbed NH_3 compared to ZS16 whereas these values for ZS16D are the lowest in the series of zeolites studied here. In contrast, its molar Al fraction (979 µmol g^{-1}) marks the highest value.

In order to better understand the acidity of hierarchical zeolite ZS16D, DRIFT spectra have been recorded (Fig. 3) linked with a temperature-programmed desorption of NH_3. Fig. 3 shows DRIFT spectra of zeolite ZS16D in the range between 3800 cm^{-1} and 2600 cm^{-1}, in each case recorded at 50 °C, before NH_3 loading and after having desorbed ammonia at different temperature steps. In addition, DRIFT spectra of commercially available zeolite A (Zeolyst CBV5524G, @50 °C under He, "unloaded" & after NH_3 desorption @50 °C) are also depicted for sake of comparison.

Thanks to many comprehensive studies dealing with IR/DRIFT spectroscopy and, particularly, with the interaction of probe molecules with the surface of zeolites [29 – 31], different regions within the O – H stretching domain can be differentiated. For instance, free terminal silanol groups located on the outer surface of the material lead to a sharp, strong absorption band at 3745 cm^{-1} according to Barbera et al. [32] whereas silanol nests, located at internal defect sites and crystal intergrowth structures, are sometimes detected as rather inconspicuous shoulders around 3400 cm^{-1}. The spectra of catalyst ZS16D (Fig. 3) shows a distinct, strong absorption band at 3741 cm^{-1} whereas the commercial benchmark zeolite A displays a clearly weaker terminal silanol ν(O – H) band at 3741 cm^{-1}. In both cases the presence of internal silanol nests could not be clearly established in the spectra: either missing in the spectra recorded with the unloaded zeolite or overlapping unfortunately with ν(N – H) in the spectra measured after NH_3 loading. The increased number of free silanol groups, in comparison to A, is expected due to the formation of mesopores during the manufacturing process, resulting in an extended external surface area [33]. This finding is in good agreement with results from related studies [20, 22, 34 – 37].

The ν(O – H) absorption bands involving more the aluminum sites can be found, for both measured zeolites, at ca. 3590 cm^{-1} for Brønsted acid sites Si-O(H)-Al [38] and at 3663 cm^{-1} for so-called extra-framework aluminum species (EFAL) that behave more like Lewis acids in agreement with already documented studies [39 – 41]. Interestingly these absorption bands are broader in the spectra originally recorded for the unloaded zeolites Z16D and A, suggesting

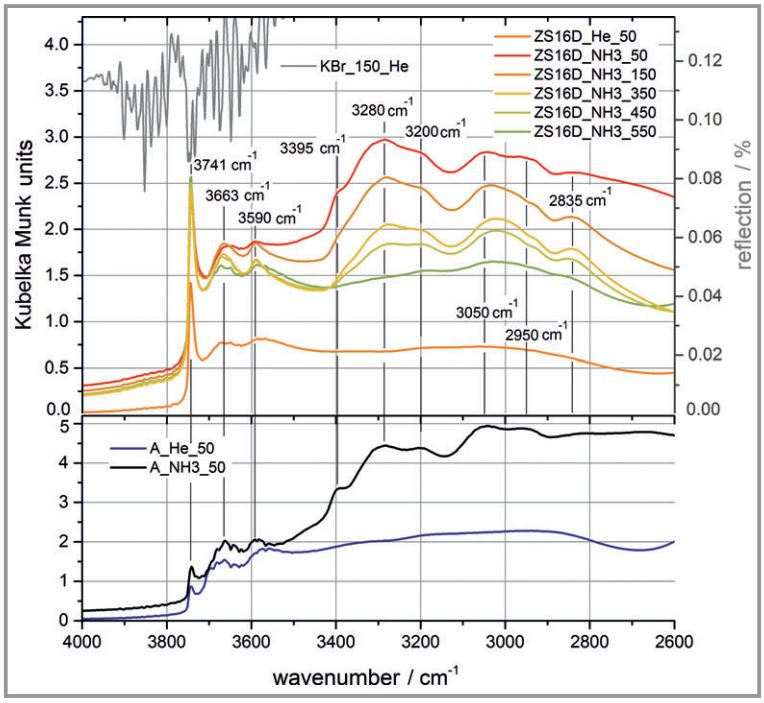

Figure 3. DRIFT spectra of catalyst ZS16D (recorded from 50 °C up to 450 °C, in 50-°C steps) as Kubelka-Munk plots (left ordinate). Plotted in blue and black are the reference spectra of Zeolite A (at 50 °C after degassing under He and at 50 °C after NH_3 loading). The right ordinate relates to the reflection spectrum of KBr (gray line on top).

the presence of water traces in the samples able to interact via H-bonds with Lewis and Brønsted sites [42]. Compared to the "unloaded" spectra, recorded in the absence of ammonia, the range between 3400 cm^{-1} and 1500 cm^{-1} display, for both zeolites Z16D and A, broad absorption bands typically connected to the presence of NH_3 interacting with the surface of the zeolites [43, 44]. This can be more precisely split in stretching bands at 3395 cm^{-1} ($\nu 3(N-H)_{asym}$) and 3280 cm^{-1} ($\nu 1(N-H)_{sym}$) and deformation bands ($\nu(N-H)$) around 1400 cm^{-1} [45, 46]. Further broad absorption bands recorded at 3050 cm^{-1} and 2850 cm^{-1} after loading with NH_3 (Fig. 3, red line) can be also tentatively attributed to NH_3 interacting weakly with Lewis- and Brønsted acidic sites [42 ,47, 48]. According to the literature the attributions in this region have to be made cautiously as pure absorption bands of differently coordinated NH_3 and Fermi resonances (from ν(NH) and overtones of the bending modes) may overlap [49]. However, some general facts can be observed: The stretching absorption bands found in the range between 3400 cm^{-1} and 2800 cm^{-1} decrease with increasing temperature as expected for a controlled desorption of NH_3 from the zeolite surface. Moreover, a qualitative trend can be observed for both zeolites involving the decrease of the absorption bands around 3300 cm^{-1} whereas the bands around 3050 cm^{-1} remain relatively constant. This change, without being spectacular, suggests an easier desorption of ammonia from the Lewis sites (broad band @ 3300 cm^{-1}) than from the Brønsted acidic sites (region between 3050 cm^{-1} and 2850 cm^{-1}) [50]. In addition, comparing the surface ratio of these regions (around 3000 cm^{-1} and around 3300 cm^{-1}) in zeolite A (Fig. 3, spectrum I) and Z16D (Fig. 3, spectrum II) suggests that zeolite A shows a higher amount of strong acidic sites than zeolite Z16D. This finding correlates with NH_3-TPD experiments described above.

N_2-physisorption isotherms of the catalysts are shown in Fig. 4. At very low relative pressures, a very steep increase is observed without exception for all isotherms, which is due to the presence of micropores. All isotherms show a hysteresis. This behavior is related to mesoporosity in the intracrystalline region. The hysteresis behavior of A and B is rather marginal and most likely caused by the intercrystalline structure. A particular conspicuousness is the range where adsorption and desorption branches are recombining (the so-called closure point) for ZS16 and ZS16D. These are found at relative pressures p/p_0 below 0.2 for ZS16 and ZS16D, whereas the closure point of all other zeolites is located at approximately 0.45. This characteristic shift is referred to as low-pressure hysteresis [51 – 53] and can be caused by various factors

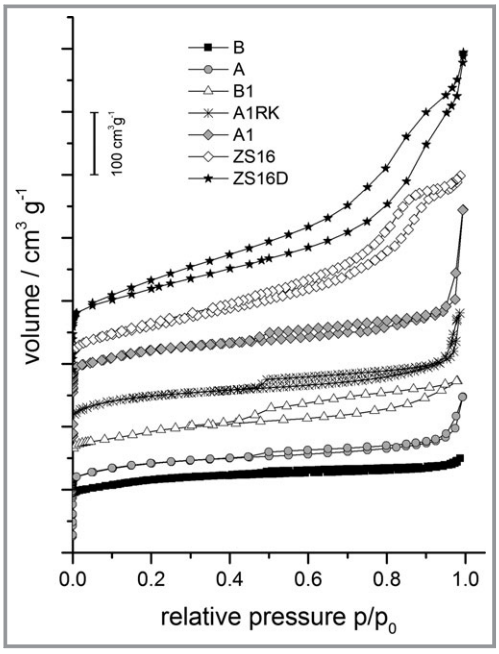

Figure 4. N_2 isotherms measured at 77 K with adsorption and desorption branches (hysteresis loops) for the tested catalysts. Individual curves are vertically offset by 100 cm^3g^{-1}.

like an insufficient equilibrium time during measurement and conditioning. Equilibration rate is typically influenced by pore network effects by incomplete emptying of the adsorbate from larger pores via smaller pores (nested convoluted porosity), observable as shift of the desorption branch. Since all zeolites were measured with the same measuring conditions, it can be concluded that ZS16 and ZS16D have a divergent pore system in comparison to the other samples.

In comparison to the unmodified zeolites A and B, the respective values for the BET surface areas (S) and external surface areas (S_{ext}) are larger for the mesoporous zeolites, with the exception of B1 (Tab. 2).

Table 2. Results of N_2 physisorption measurements, values calculated by BET model, t-plot, and BJH.

Zeolite	S (BET*) [m^2g^{-1}]	V_{micro} (t-plot) [cm^3g^{-1}]	S_{ext} (t-plot) [m^2g^{-1}]	V_{meso} ($BJH_{Ads.}$) [cm^3g^{-1}]	S_{ext}/V_{meso} [10^4 cm^{-1}]
A	427	0.145	83	0.08	1038
A1	488	0.163	116	0.13	892
B	426	0.150	70	0.04	1750
B1	423	0.128	127	0.13	1000
A1RK	457	0.150	97	0.11	977
ZS16	481	0.075	310	0.40	775
ZS16D	452	0.046	355	0.52	682

*BET evaluation range p/p_0 = 0.003 – 0.128.

For A1 and A1RK, the micropore volume is increased with respect to A. This effect has previously been explained by pore blocking [34]. Structural changes due to desilication, which are already mentioned, are also an explanation for these experimental findings, as expansion of micropores by preferential dissolution of atoms in certain positions of the framework is possible.

Generally, the combination of effects such as pore blocking, varying amorphous parts, and measurement-induced error sources (e.g., sample weight) complicates the discussion of physisorption results. This may lead to misinterpretations. For characterization of mesoporosity, the numerical and weight-independent ratio of mesopore surface area to mesopore volume, hereinafter referred to S_{ext}/V_{meso}, is suitable. Furthermore, conclusions on the geometry of the mesopores can be derived. In Tab. 2 the ratios of external surfaces (t-plot) to cumulative mesopore volumes in the pore radius range between 3 and 50 nm according to BJH are listed. A decreasing S_{ext}/V_{meso} ratio means an increase in the pore diameter. Correspondingly, S_{ext}/V_{meso} is reduced for A1, B1 and A1RK compared to A and B. Furthermore, the zeolites ZS16 and ZS16D have the smallest values, corresponding to larger mesopore diameters, among the zeolites investigated here. In ZS16D, S_{ext}/V_{meso} decreases with respect to ZS16 due to the effects of desilication, which is plausible by growing mesopore radii.

3.2 Catalyst Testing

The experimentally found DME conversion as a function of *TOS* (solid lines) for all catalysts are shown in Fig. 5. The curves originating from Janssens' model with adjusted rate coefficients k and deactivation coefficients a are depicted as dashed lines. Compared to A and B, the zeolites A1, A1RK, and B1 show lower k values, which is associated with reduced activity according to Janssens' model (see Sect. 2.8).

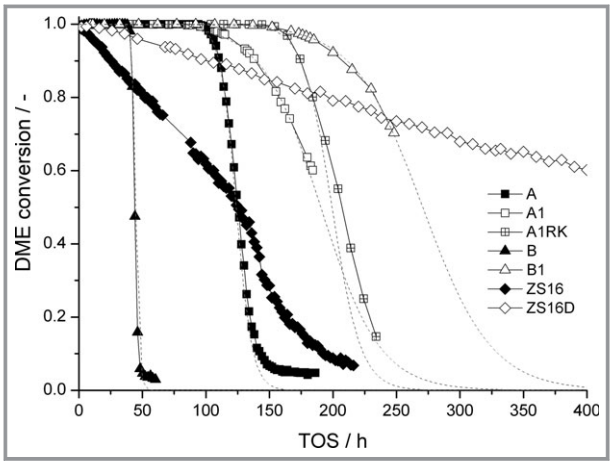

Figure 5. DME conversion vs. time on stream (*TOS*) for A, A1, A1RK, B, B1, ZS16, and ZS16D. The dashed lines represent the computed curves by Janssens' model.

For DME conversion with ZS16 and ZS16D Janssens' model cannot be applied, because the function does not show an inverse S-shape. Nevertheless, an estimation of the order of magnitude of k and a is possible due to their decreasing DME conversion starting at *TOS* = 0 h. Thus, the values for k of ZS16 and ZS16D are estimated to be between 3 and 8 mol $g^{-1}h^{-1}$.

These low rate coefficients are in accordance with the comparatively low values of $NH_{3,HTR}$, which can be related to the catalytically relevant Brønsted acid centers. Noteworthy is the $NH_{3,HTR}$ value of A1RK (500 µmol g^{-1}), which is higher than that of the starting material A (358 µmol g^{-1}). Interestingly, this is not associated with an increased activity of A1RK, which is evident from a lower rate coefficient k in comparison to A (Tab. 3). From this observation it can be concluded that not only the quantity but also the quality (chemical environment, density, accessibility, etc.) of the existing active acid centers is important for the DME conversion behavior.

In all cases, a significantly reduced value for a is calculated for the desilicated zeolites (Tab. 3). The high conversion capacities R_0, resulting from Janssens' model, are consequently attributed to reduced coefficients a and not to increased rate coefficients k, according to the idea that the catalyst has only few active centers, keeping their activity for a long period (long average activity period). Large values for a and k represent catalysts with numerous active centers, however, they become more rapidly inactive (short average activity period). Hierarchical zeolites (A1, A1RK, B1, ZS16D) have a significantly longer average activity period compared to A, B, and ZS16 and correspondingly higher conversion capacities R_0.

Based on the concept of Janssens' model, the impact of a increases and the relevance of k decreases with increasing residence time $\tau_{mod,0}$ for achieving high conversion capacities R_0. As a consequence, ZS16D with the highest R_0 should show the longest *TOS* at 100 % conversion, as long as $\tau_{mod,0}$ is sufficiently high with all other parameters being constant.

For 24 h *TOS*, zeolite A shows a constant selectivity (Fig. 6) for the products ethylene, propane, propylene, C5, C4/MeOH, C6 – C9 and C10+. The selectivity to propylene steadily increases after 24 h. It is well-known that the yield of propylene is unstable at high conversion rates [54]. After 120 h (DME conversion of approximately 70 %, Fig. 5) the selectivity to the fractions C6 – C9 and C10+ increases significantly, while the selectivity to propylene and C4/MeOH decreases. At low DME conversion it can be assumed that reactant molecules are present in excess at the remaining active centers, leading to an increased build-up of higher hydrocarbons. The increasing selectivity of the fraction C4/MeOH with decreasing DME conversion after 110 h is owed to partial conversion to MeOH. In the case of A1 (Fig. 6) similar selectivities compared to A are determined at the beginning (*TOS* < 24 h). The selectivity of propane and the fraction C4/MeOH are diminished compared to A,

Table 3. Compilation of experimental conditions with amount of catalyst used, residence time *WHSV*, and rate coefficient *k*, deactivation coefficient *a*, and conversion capacity R_0 determined from Janssens' model for catalysts A, A1, B, B1, A1RK, ZS16, and ZS16D.

Catalyst	A	A1	B	B1	A1RK	ZS16	ZS16D
Quantity used [a] [mg]	200	200	200	200	200 (186)	200 (160)	200 (182)
Residence time $\tau_{mod,0}$ [a] [g h mol^{-1}]	0.51	0.51	0.51	0.51	0.51 (0.48)	0.51 (0.41)	0.51 (0.47)
WHSV [a] [$g_{DME}g_{cat}^{-1}h^{-1}$]	3.25	3.25	3.25	3.25	3.25 (3.49)	3.25 (4.06)	3.25 (3.57)
Rate coefficient *k* [mol g^{-1}h^{-1}]	44	16	60	19.5	37	3 – 8	4 – 6
Deactivation coefficients *a* [10^{-3} · g mol^{-1}]	4,2	2.7	11.5	1.9	2.4	3 – 4	~1
Conversion capacity R_0 [a, b] [$g_{DME}g_{cat}^{-1}$]	406	618	143	878	670 (719)	406 (508)	1706 (1874)

a) The values in parentheses are taking the respective crystallinity into account (calculated from quantity of catalyst used and crystallinity value, SI_{XRD}. Values above 100 % were not considered and assumed to be 100 % crystalline.) b) Determined from Janssens' model (multiplication of *WHSV* with the measured or extrapolated *TOS* at which 50 % conversion was achieved).

while the selectivities of propylene and the fraction C10+ are increased. After 30 h, increase of C6 – C9 and propylene becomes apparent, as the share of C4/MeOH decreases. Analogous observations are made for B and B1 (see SI), with altered course of time. In particular, increase of the fraction C6 – C9 at full conversion is a typical feature of hierarchical catalysts [55 – 58].

The *TOS*-depending change for the product fractions C6 – C9 (increase) and C4/MeOH (decrease) with catalysts A1 and B1 are consistent with the declining ΔT of the axial reactor temperature profiles at 100 % DME conversion. The questions arises whether the differences in selectivity are influenced by catalysts properties since temperature shifts as well as varying DME conversion also have to be taken into account as possible causes. For instance, with catalyst A1RK (see SI), which shows the highest ΔT of approximately 4 K, selectivities to ethylene and the C6 – C9 fraction are slightly lower at short *TOS* values compared to catalyst A, whereas on the other hand propylene selectivity is increased. A higher temperature is typically applied to obtain olefins, which is in accordance with this result.

Catalysts ZS16 and ZS16D (see SI) show high initial selectivity to propylene (> 25 %) which declines with increasing *TOS*. Selectivity to C6 – C9 is significantly increased and remains above 32 % (with the exception of one outlying data point) during the entire duration of the experiments. This is because both catalysts show declining DME conversion from the start which is accompanied by changes in selectivity as mentioned above.

For comparability of catalytic testing results, a small axial temperature gradient (375 °C, 1 bar) is required, since kinetics (selectivity) and deactivation mechanism are influenced by the temperature [59, 60]. Depending on the reaction conditions (τ_{mod}, *p*, *T*, *WHSV*), hot spots within the catalyst bed are possible. It is known that the conversion of MeOH at H-ZSM-5 catalysts takes place in a narrow reaction zone which is moving through the catalyst bed during the runtime comparable to a burning cigar [61].

The time-dependent temperature profiles along the catalyst beds are shown at different *TOS* and corresponding DME conversions using the examples of catalysts A, A1, ZS16D, and B (Fig. 7). In all experiments, the axial temperature differences ΔT ($T_{max} - T_{min}$) of the catalyst beds of A, A1, ZS16D, and B as well as B1, A1RK, and ZS16 (see SI) are varying in an interval of less than or equal to 4 K. For catalyst A and A1RK, this ΔT rises to 4 K, whereas the other catalysts do not reach equally high ΔT. It is therefore assumed that the investigated catalysts are similarly deactivated.

For the purely microporous zeolite A (Fig. 7, top left), a temperature profile with a pronounced temperature

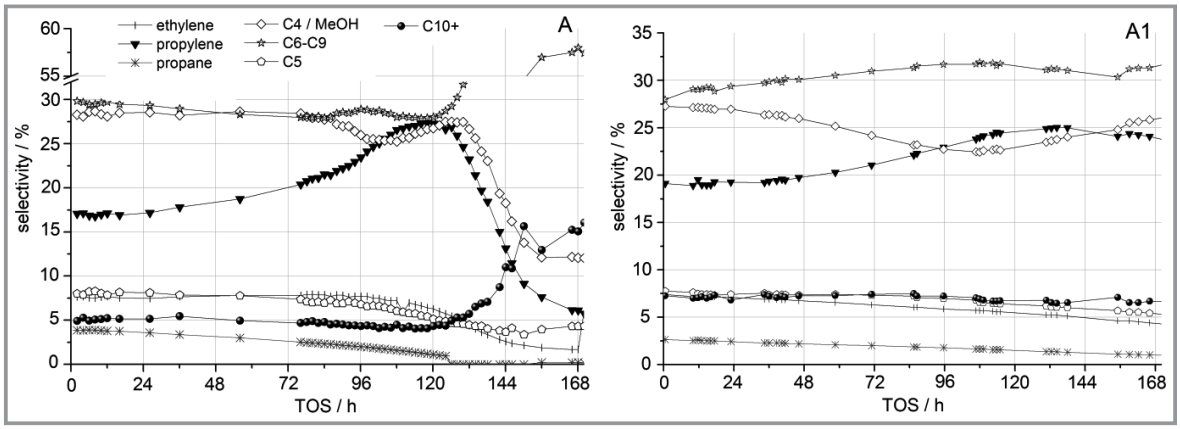

Figure 6. Selectivities vs. *TOS* of zeolite A and A1.

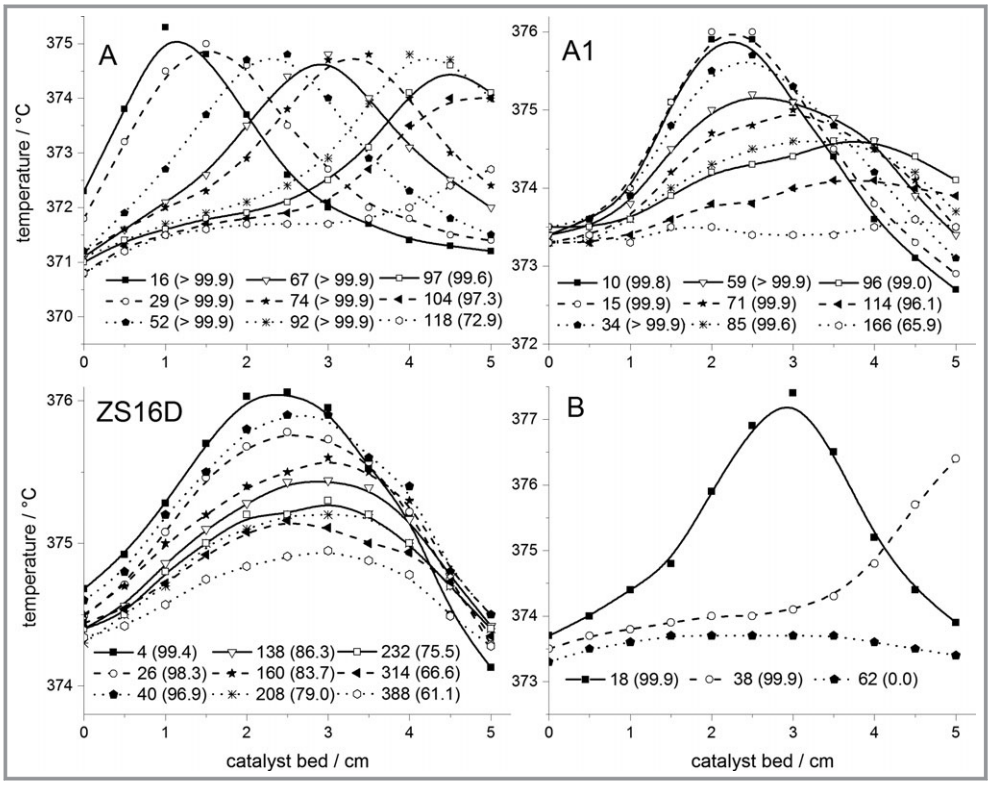

Figure 7. Temperature profiles along the catalyst bed of catalyst A, A1, ZS16D, and B at different *TOS*. The first number gives the *TOS*, DME conversion is given in parentheses.

maximum is apparent, with a maximum shifting with slightly changing ΔT at increasing *TOS* and constant DME conversion of 100 % (*TOS* < 92 h) along the catalyst bed. With lowered DME conversion (*TOS* > 92 h), ΔT decreases at the end of the catalyst bed.

A1 (Fig. 7, top right) also shows a temperature profile with one temperature maximum, which is decreasing with increasing *TOS* and is gradually shifted to the end of the bed, accompanied by a broadening of the temperature profile. At a *TOS* of 59 h, conversion is still almost 100 %, with lower ΔT compared to its initial value. Similar observations are made for A1RK and B1 (see SI).

The temperature maximum of ZS16D (Fig. 7, bottom left) is almost in the middle of the catalyst bed. With increasing *TOS*, the maximum decreases, staying nearly at its initial axial position according to decreasing DME conversion. Correspondingly, analogous findings for ZS16 support this hypothesis (see SI).

In the case of the unmodified catalyst B (Fig. 7, bottom right), a similarly shift of the temperature maximum with increasing *TOS* is observed, but in contrast to A, with decreasing maximum although the catalyst still achieves full DME conversion. Catalyst B has higher activity in the sense of Janssens' model (k) compared to A, although, this is not reflected from the temperature profile. An explanation could be the fact that B has a lower Al content and thereby a lower overall acidity compared to A.

Assuming coking of the catalyst is taking place in the bed region with increased temperature, profiles shown here allow an indirect conclusion on the coke distribution in the catalyst bed. Bleken et al. [62] found different coke distributions for MtG on the catalyst bed for unmodified and mesoporous H-ZSM-5. The described coke distributions correlate well with the temperature profiles of the DtG experiments presented here. The assumption mentioned above is confirmed, on the basis of the similar measuring results. Based on the temperature profile with catalyst A (Fig. 7, top left) it is supposed that the coke is predominantly formed after 16 h *TOS* in the initial reactor volume (2 cm). In contrast, a more uniform distribution of the deposited coke is attributed to the temperature profile of ZS16D (Fig. 7, bottom left) and ZS16 (SI) after 30 h *TOS*. By means of TGA (see SI) it was proven that despite the fact of a longer *TOS* (approx. 350 %) with ZS16D less C-containing deposits (6 wt %) are present than with catalyst A.

4 Conclusions

The analytical results from XRD and N_2 physisorption measurements suggest the possibility of a systematic transformation of the framework structure via desilication. The structural parameters of the unit cell also affect the chemical surrounding of the active sites. Furthermore, the calcination process significantly influences the acid sites, depending on the ambient gas composition.

The combination of an organosilane-directed synthesis with subsequent desilication results in the highest DME

conversion capacity (1700 $g_{DME}g_{cat}^{-1}$) of all of the tested catalysts described in this work. Thus, not only the quantity but also the quality (localization and strength) of the acidic sites is important. The testing of mesoporous H-ZSM-5 in the tubular reactor shows a broadening of the temperature profile along the catalyst bed. The Janssens model has proven to be a good method for distinguishing differences in catalytic activity and coking behavior and allows an easier evaluation of the system. The activity as defined by Janssens' model was lowered in each case of the modified mesoporous materials. This is a starting point for future catalysts and necessitates more detailed characterization of the acid sites, combined with new methodological approaches.

The characteristics of hierarchical ZSM-5 are manifold: acidity, crystallinity, defect sites, intergrowth, crystal size, micropore and mesopore surface and volume. The goal is a catalyst with a high yield of the fraction C6 – C9 and simultaneously low coking tendency. Therefore, a catalyst – in particular a hierarchical H-ZSM-5 – with a high content of strong acid centers and a low content of weak acid centers appears to be promising. However, the complex interaction of all catalytically active parameters in their entirety represents the actual driving force in the conversion of dimethyl ether to hydrocarbons. Along these lines an optimized process management, especially a controlled temperature profile, plays a significant role since even small temperature changes greatly affect the deactivation mechanism as well as the selectivity.

We thank Dr.-Ing. U. Ohlrogge (Zeolysts International), Mrs. D. Neumann-Walter (N_2 physisorption), Dr. U. Arnold, D. Warskovich, Dr. A. Hahn (ZetA Partikelanalytik, Mainz) and Dr. V. Hagen (Rubokat) for supporting this work.

Symbols used

a	$[10^{-3} \cdot g\,mol^{-1}]$	deactivation coefficients
k	$[mol\,g^{-1}h^{-1}]$	rate coefficient
KM	[–]	Kubelka Munk
m_{cat}	[g]	catalyst mass
p	[bar]	pressure
p_0	[bar]	saturation vapor
p/p_0	[–]	relative pressure
r	[° 2θ]	reflection
R_0	$[g_{DME}g_{cat}^{-1}]$	conversion capacity
S	$[m^2g^{-1}]$	surface
S_{ext}	$[m^2g^{-1}]$	external surface
S_{KBr}	[–]	KBr background spectra
S_{prod}	[–]	product selectivity
S_r	[–]	counting pulses of the reference signal
S_{sample}	[–]	sample spectra
S_X	[–]	counting pulses of the sample signal
SI_{XRD}	[%]	relative crystallinity
T	[K]	temperature
T_{max}	[K]	temperature maximum
T_{min}	[K]	temperature minimum
TOS	[h]	time on stream
V_{meso}	$[cm^3g^{-1}]$	mesoporous volume
V_{micro}	$[cm^3g^{-1}]$	micropore volume
V_{total}	[%]	total volume flow
$WHSV$	$[g_{DME}g_{cat}^{-1}h^{-1}]$	weight hourly space velocity
X	[%]	conversion

Greek letters

$\tau_{mod,0}$	$[g\,h\,mol^{-1}]$	residence time
ν	$[cm^{-1}]$	wave number
φ_i	[%]	volume fraction

Abbreviations

A	CBV5524G (commercial ZSM-5, Zeolyst International)
A1	CBV5524G treated with 0.1 M NaOH solution, calcined under air
A1RK	A1 calcined under Ar
B	CBV8014 (commercial ZSM-5, Zeolyst International)
B1	CBV8014 treated with 0.1 M NaOH solution, calcined under air
BET	Brunauer-Emmett-Teller
BJH	Barrett-Joyner-Halenda
C4	hydrocarbons with 4 C atoms
C5	hydrocarbons with 5 C atoms
C6 – C9	hydrocarbons between 6 C atoms and 9 C atoms
C10+	hydrocarbons with 10 C atoms and higher
DME	dimethyl ether
DRIFTS	diffuse reflectance infrared Fourier transform spectroscopy
DtG	dimethyl ether to gasoline
FID	flame ionization detector
ICP-OES	inductively coupled plasma optical emission spectrometry
MeOH	methanol
MtG	methanol to gasoline
PTFE	polytetrafluorethylene
PXRD	powder X-ray diffraction
TGA	thermogravimetric analysis
TPABr	tetrapropylammonium bromide
TPD	temperature-programmed desorption
TPHAC	[3(trimethoxysilyl)propyl]hexadecyldimethyl-ammonium chloride
ZS16	organosilane-based ZSM-5
ZS16D	desilicated organosilane-based ZSM-5
ZSM-5	zeolite Socony Mobil-5

References

[1] T. Mokrani, M. Scurrell, *Catal. Rev.* **2009**, *51 (1)*, 1 – 145. DOI: https://doi.org/10.1080/01614940802477524

[2] G. Kreysa, *Chem. Unserer Zeit* **2010**, *44 (5)*, 332 – 338. DOI: https://doi.org/10.1002/ciuz.201000529

[3] N. Dahmen, J. Abeln, M. Eberhard, T. Kolb, H. Leibold, J. Sauer, D. Stapf, B. Zimmerlin, *Wiley Interdiscip. Rev.: Energy Environ.* **2017**, *6 (3)*, e236. DOI: https://doi.org/10.1002/wene.236

[4] S. Svelle, S. Kolboe, O. Swang, U. Olsbye, *J. Phys. Chem. B* **2005**, *109 (26)*, 12874 – 12878. DOI: https://doi.org/10.1021/jp051125z

[5] J. S. Martinez-Espin, M. Mortén, T. V. W. Janssens, S. Svelle, P. Beato, U. Olsbye, *Catal. Sci. Technol.* **2017**, *7*, 2700 – 2716. DOI: https://doi.org/10.1039/c7cy00129k

[6] D. Rojo-Gama, M. Nielsen, D. S. Wragg, M. Dyballa, J. Holzinger, H. Falsig, L. F. Lundegaard, P. Beato, R. Y. Brogaard, K. P. Lillerud, U. Olsbye, S. Svelle, *ACS Catal.* **2017**, *7*, 8235 – 8246. DOI: https://doi.org/10.1021/acscatal.7b02193

[7] C. D. Chang, *Catal. Rev.* **1983**, *25 (1)*, 1 – 118. DOI: https://doi.org/10.1080/01614948308078874

[8] U. Olsbye, S. Svelle, M. Bjørgen, P. Beato, T. V. W. Janssens, F. Joensen, S. Bordiga, K. P. Lillerud, *Angew. Chem., Int. Ed.* **2012**, *51 (24)*, 5810 – 5831. DOI: https://doi.org/10.1002/anie.201103657

[9] R. Chal, C. Gérardin, M. Bulut, S. van Donk, *ChemCatChem* **2011**, *3 (1)*, 67 – 81. DOI: https://doi.org/10.1002/cctc.201000158

[10] L.-H. Chen, X.-Y. Li, J. C. Rooke, Y.-H. Zhang, X.-Y. Yang, Y. Tang, F.-S. Xiao, B.-L. Su, *J. Mater. Chem.* **2012**, *22 (34)*, 17381 – 17403. DOI: https://doi.org/10.1039/C2JM31957H

[11] D. P. Serrano, J. M. Escola, P. Pizarro, *Chem. Soc. Rev.* **2013**, *42 (9)*, 4004 – 4035. DOI: https://doi.org/10.1039/C2CS35330J

[12] K. Na, M. Choi, R. Ryoo, *Microporous Mesoporous Mater.* **2013**, *166*, 3 – 19. DOI: https://doi.org/10.1016/j.micromeso.2012.03.054

[13] W. Schwieger, A. G. Machoke, T. Weissenberger, A. Inayat, T. Selvam, M. Klumpp, A. Inayat, *Chem. Soc. Rev.* **2016**, *45 (12)*, 3305 – 3566. DOI: https://doi.org/10.1039/c5cs00599

[14] D. Verboekend, S. Mitchell, M. Milina, J. C. Groen, J. Pérez-Ramírez, *J. Phys. Chem. C* **2011**, *115 (29)*, 14193 – 14203. DOI: https://doi.org/10.1021/jp201671s

[15] M. Choi, H. S. Cho, R. Srivastava, C. Venkatesan, D. H. Choi, R. Ryoo, *Nat. Mater.* **2006**, *5 (9)*, 718 – 723. DOI: https://doi.org/10.1038/nmat1705

[16] M. Hartmann, *Angew. Chem.* **2004**, *116 (44)*, 6004 – 6006. DOI: https://doi.org/10.1002/ange.200460644

[17] D. Schneider, D. Mehlhorn, P. Zeigermann, J. Kärger, R. Valiullin, *Chem. Soc. Rev.* **2016**, *45*, 3439 – 3467. DOI: https://doi.org/10.1039/c5cs00715a

[18] M. Ogura et al., *Chem. Lett.* **2000**, *29 (8)*, 882 – 883. DOI: https://doi.org/10.1246/cl.2000.882

[19] M. Milina, S. Mitchell, D. Cooke, P. Crivelli, J. Pérez-Ramírez, *Angew. Chem., Int. Ed.* **2015**, *54*, 1591 – 1594. DOI: https://doi.org/10.1002/anie.201410016

[20] S. Svelle, L. Sommer, K. Barbera, P. N. R. Vennestrøm, U. Olsbye, K. P. Lillerud, S. Bordiga, Y.-H. Pan, P. Beato, *Catal. Today* **2011**, *168 (1)*, 38 – 47. DOI: https://doi.org/10.1016/j.cattod.2010.12.013

[21] A. J. J. Koekkoek, C. H. L. Temelmann, V. Degirmenci, M. Guo, Z. Feng, C. Li, E. J. M. Hensen, *Catal. Today* **2011**, *168 (1)*, 96 – 111. DOI: https://doi.org/10.1016/j.cattod.2010.12.033

[22] D. P. Serrano, R. A. García, M. Linares, B. Gil, *Catal. Today* **2012**, *179 (1)*, 91 – 101. DOI: https://doi.org/10.1016/j.cattod.2011.06.029

[23] D. Tzoulaki, A. Jentys, J. Pérez-Ramírez, K. Egeblad, J. A. Lercher, *Catal. Today* **2012**, *198 (1)*, 3 – 11. DOI: https://doi.org/10.1016/j.cattod.2012.03.078

[24] T. V. W. Janssens, *J. Catal.* **2009**, *264 (2)*, 130 – 137. DOI: https://doi.org/10.1016/j.jcat.2009.03.004

[25] DIN ISO 9277:2010, *Bestimmung der spezifischen Oberfläche von Festkörpern mittels Gasadsorption – BET-Verfahren*, Beuth Verlag, Berlin **2014**.

[26] B. C. Lippens, J. H. de Boer, *J. Catal.* **1965**, *4 (3)*, 319 – 323. DOI: https://doi.org/10.1016/0021-9517(65)90307-6

[27] DIN 66134, *Determination of the pore size distribution and the specific surface area of mesoporous solids by means of nitrogen sorption – Method of Barrett, Joyner and Halenda (BJH)*, Beuth Verlag, Berlin **1998**.

[28] B. Gil, L. Mokrzycki, B. Sulikowski, Z. Olejniczak, S. Walas, *Catal. Today* **2010**, *152 (1 – 4)*, 24 – 32. DOI: https://doi.org/10.1016/j.cattod.2010.01.059

[29] K. Sadowska, K. Góra-Marek, J. Datka, *Vib. Spectrosc.* **2012**, *63*, 418 – 425. DOI: https://doi.org/10.1016/j.vibspec.2012.09.007

[30] T. Fujino, M. Kashitani, J. N. Kondo, K. Domen, C. Hirose, M. Ishida, F. Goto, F. Wakabayashi, *J. Phys. Chem.* **1996**, *100*, 11649 – 11653. DOI: https://doi.org/10.1021/jp953127x

[31] F. Wakabayashi, J. N. Kondo, K. Domen, C. Hirose, *Catal. Lett.* **1996**, *38*, 15 – 19. DOI: https://doi.org/10.1007/BF00806893

[32] K. Barbera, F. Bonino, S. Bordiga, T. V. W. Janssens, P. Beato, *J. Catal.* **2011**, *280 (2)*, 196 – 205. DOI: https://doi.org/10.1016/j.jcat.2011.03.016

[33] H. V. Brand, A. Redondo, P. J. Hay, *J. Mol. Catal. A: Chem.* **1997**, *121*, 45 – 62. DOI: https://doi.org/10.1016/S1381-1169(96)00456-6

[34] K. Sadowska, A. Wach, Z. Olejniczak, P. Kuśtrowski, J. Datka, *Microporous Mesoporous Mater.* **2013**, *167*, 82 – 88. DOI: https://doi.org/10.1016/j.micromeso.2012.03.045

[35] D. Verboekend, J. Pérez-Ramírez, *Chem. – Eur. J.* **2011**, *17 (4)*, 1137 – 1147. DOI: https://doi.org/10.1002/chem.201002589

[36] K. Sadowska, K. Góra-Marek, M. Drozdek, P. Kuśtrowski, J. Datka, J. Martinez Triguero, F. Rey, *Microporous Mesoporous Mater.* **2013**, *168*, 195 – 205. DOI: https://doi.org/10.1016/j.micromeso.2012.09.033

[37] J. C. Groen, J. A. Moulijn, J. Pérez-Ramírez, *J. Mater. Chem.* **2006**, *16 (22)*, 2121 – 2131. DOI: https://doi.org/10.1039/b517510k

[38] Z. Xue, T. Zhang, J. Ma, H. Miao, W. Fan, Y. Zhang, R. Li, *Microporous Mesoporous Mater.* **2012**, *151*, 271 – 276. DOI: https://doi.org/10.1016/j.micromeso.2011.10.026

[39] W. E. Farneth, R. J. Gorte, *Chem. Rev.* **1995**, *95 (3)*, 615 – 635. DOI: https://doi.org/10.1021/cr00035a007

[40] H. Matsuura, N. Katada, M. Niwa, *Microporous Mesoporous Mater.* **2003**, *66*, 283 – 296. DOI: https://doi.org/10.1016/j.micromeso.2003.09.020

[41] P. Bräuer, P. Ling Ng, O. Situmorang, I. Hitchcock, C. D'Agostino, *RSC Adv.* **2017**, *7*, 52604 – 52613. DOI: https://doi.org/10.1039/c7ra10699h

[42] F. Wakabayashi, J. N. Kondo, K. Domen, C. Hirose, *Catal. Lett.* **1996**, *38*, 15 – 19. DOI: https://doi.org/10.1007/BF00806893

[43] K. Suzuki, T. Noda, N. Katada, M. Niwa, *J. Catal.* **2007**, *250*, 151 – 160. DOI: https://doi.org/10.1016/j.jcat.2007.05.024

[44] R. Barthos, F. Lónyi, Gy. Onyestyák, J. Valyon, *J. Phys. Chem. B* **2000**, *104*, 7311 – 7319. DOI: https://doi.org/10.1021/jp000937m

[45] M. Takeuchi, T. Tsukamoto, A. Kondo, M. Matsuoka, *Catal. Sci. Technol.* **2015**, *5*, 4587 – 4593. DOI: https://doi.org/10.1039/c5cy00753d

[46] F. Yin, A. L. Blumenfeld, V. Gruver, J. J. Fripiat, *J. Phys. Chem. B* **1997**, *101*, 1824 – 1830. DOI: https://doi.org/10.1021/jp9618542

[47] G. M. Robb, W. Zhang, P. G. Smirniotis, *Microporous Mesoporous Mater.* **1998**, *20*, 307 – 316. DOI: https://doi.org/10.1016/S1387-1811(97)00026-7

[48] J. B. Uytterhoeven, L. G. Christner, W. K. Hall, *J. Phys. Chem.* **1965**, *69*, 2117 – 2126. DOI: https://doi.org/10.1021/j100890a052

[49] A. Zecchina, L. Marchese, S. Bordiga, C. Pazè, E. Gianotti, *J. Phys. Chem. B* **1997**, *101*, 10128 – 10135. DOI: https://doi.org/10.1021/jp9717554
[50] A. S. Al-Dughaither, H. de Lasa, *Ind. Eng. Chem. Res.* **2014**, *53*, 15303 – 15316. DOI: https://doi.org/10.1021/ie4039532
[51] E. Panayi, C. Theocharis, in *Characterisation of Porous Solids VIII: Proceedings of the 8th International Symposium on the Characterisation of Porous Solids* (Eds: S. Kaskel et al.), The Royal Society of Chemistry, Cambridge **2009**, Ch. 24.
[52] A. M. Silvestre-Albero, J. M. Juárez-Galán, J. Sivestre-Alberto, F. Rodriguez-Reinoso, *J. Phys. Chem. C* **2012**, *116 (31)*, 16652 – 16655. DOI: https://doi.org/10.1021/jp305358y
[53] C. Reichenbach, D. Enke, J. Möllmer, D. Klank, M. Klauck, G. Kalies, *Microporous Mesoporous Mater.* **2013**, *181*, 68 – 73. DOI: https://doi.org/10.1016/j.micromeso.2013.07.007
[54] F. L. Bleken, T. V. W. Janssens, S. Svelle, U. Olsbye, *Microporous Mesoporous Mater.* **2012**, *164*, 190 – 198. DOI: https://doi.org/10.1016/j.micromeso.2012.06.020
[55] M. Bjørgen, F. Joensen, M. Sprangsberg Holm, U. Olsbye, K.-P. Lillerud, S. Svelle, *Appl. Catal., A* **2008**, *345 (1)*, 43 – 50. DOI: https://doi.org/10.1016/j.apcata.2008.04.020
[56] Z. Xue, T. Zhang, J. Ma, H. Miao, W. Fan, Y. Zhang, R. Li, *Microporous Mesoporous Mater.* **2012**, *151*, 271 – 276. DOI: https://doi.org/10.1016/j.micromeso.2011.10.026
[57] G. Lietz, K. H. Schnabel, C. Peuker, T. Gross, W. Storek, J. Volter, *J. Catal.* **1994**, *148 (2)*, 562 – 568. DOI: https://doi.org/10.1006/jcat.1994.1242
[58] F. Schmidt et al., *Microporous Mesoporous Mater.* **2013**, *165*, 148 – 157. DOI: https://doi.org/10.1016/j.micromeso.2012.07.045
[59] H. Schulz, *Catal. Today* **2010**, *154 (3 – 4)*, 183 – 194. DOI: https://doi.org/10.1016/j.cattod.2010.05.012
[60] H. Schulz, M. Wei, *Top. Catal.* **2013**, *57 (6)*, 683 – 692. DOI: https://doi.org/10.1007/s11244-013-0225-9
[61] J. F. Haw, D. M. Marcus, *Top. Catal.* **2005**, *34 (1)*, 41 – 48. DOI: https://doi.org/10.1007/s11244-005-3798-0
[62] F. L. Bleken, K. Barbera, F. Bonino, U. Olsbye, K. P. Lillerud, S. Bordiga, P. Beato, T. V. W. Janssens, S. Svelle, *J. Catal.* **2013**, *307*, 62 – 73. DOI: https://doi.org/10.1016/j.jcat.2013.07.004

